Tensegrity Behavior of Cortical and Cytosolic Cytoskeletal Components in Twisted Living Adherent Cells

Valérie Laurent, Patrick Cañadas, Redouane Fodil, Emmanuelle Planus, Atef Asnacios, Sylvie Wendling, Daniel Isabey

TENSEGRITY BEHAVIOUR OF CORTICAL AND CYTOSOLIC CYTOSKELETAL COMPONENTS IN TWISTED LIVING ADHERENT CELLS

Valérie M. Laurent[1,3,5], Patrick Cañadas[1,2], Redouane Fodil[1], Emmanuelle Planus[1], Atef Asnacios[3], Sylvie Wendling[2,4] and Daniel Isabey[1,6]

[1]INSERM UMR 492, Facultés de Médecine et des Sciences et Technologies, Université Paris XII, Créteil, 94010, France.
[2]CNRS UPR 7052-B2OA, Faculté des Sciences et Technologies, Université Paris XII, Créteil, 94010, France.
[3]CNRS UPR 7057-LBHP, Université Paris VI et VII, PARIS 75252, France.
[4]CNRS UPR 7051- LMA-Marseille, 13402, France.
[5]LBBC-EPFL, PSE-A Ecublens, Lausanne, CH-1015, Switzerland.
[6] Corresponding author: Daniel Isabey, INSERM UMR 492, Fonctions Cellulaires et Moléculaires de l'Appareil Respiratoire et des Vaisseaux, Equipe Biomécanique Respiratoire et Cellulaire, Faculté de Médecine–Université Paris XII, 8 rue du Général Sarrail, 94010 Créteil Cedex, France. Tél.: 33 149 813700. Fax: 33 148 981777. Email: daniel.isabey@creteil.inserm.fr

Keywords: structural model, cytoskeleton, actin network, magnetic twisting cytometry.

ABSTRACT

The present study is an attempt to relate the multicomponent response of the cytoskeleton (CSK), evaluated in twisted living adherent cells, to the heterogeneity of the cytoskeletal structure evaluated both experimentally by means of 3D reconstructions, and theoretically considering the predictions given by two tensegrity models composed of (four and six) compressive elements and (respectively 12 and 24) tensile elements. Using magnetic twisting cytometry in which beads are attached to integrin receptors linked to the actin CSK of living adherent epithelial cells, we specifically measured the elastic CSK response at quasi equilibrium state and partitioned this response in terms of cortical and cytosolic contributions with a two component model (i.e., a series of two Voigt bodies). These two CSK components were found to be prestressed and exhibited a stress hardening response which both characterize tensegrity behaviour with however significant differences: compared to the cytosolic component, the cortical cytoskeleton appears to be a faster responding component, being a less prestressed and easily deformable structure. The discrepancies in elastic behaviour between the cortical and cytosolic CSK components may be understood on the basis of prestress tensegrity model predictions, given that the length and number of constitutive actin elements are taken into account.

1. INTRODUCTION

Transmission of mechanical forces throughout the cell induces alterations in cell shape and structure which play a critical role in the control of many cellular functions, including growth, motility, migration and mechanotransduction (Huang and Ingber, 2002; Shafrir and Forgacs, 2002). These interactions between mechanical forces/structure/function are known to be mediated through changes in the internal cytoskeleton (CSK), a network of interconnected biopolymers, which has previously been recognized as ensuring the physical linkage between the nucleus and the surface adhesion receptors (Maniotis *et al*., 1997; Janmey, 1998). Thus, understanding the role of mechanical forces in cell regulation requires consideration of the complex links between mechanical response, microstructure and molecular biochemistry. Different mechanical models have been proposed to describe the cell behaviour. Engineering models initially considered the cell as a continuum containing an elastic cortex that surrounds an elastic (Evans and Yeung, 1989) or viscoelastic (Schmid-Schonbein *et al*., 1995) cytoplasmic fluid, including eventually a viscoelastic nucleus (Dong *et al*., 1991; Caille *et al*., 2002). These models provide mechanical properties based on accurate fitting of experimental data but they are unable to distinguish the role of molecular structures notably the CSK, and therefore render the understanding of the linkage between cellular mechanics, microstructure and function difficult.

In contrast, prestress tensegrity structure has been proposed as a common principle of mechanical/geometrical interplay for a number of living organisms and particularly for cells and tissues (Ingber, 1993, 1997, 2000; Wang *et al*., 1993; Ingber *et al*., 1994; Maniotis *et al*., 1997; Chicurel *et al*., 1998; Chen and Ingber, 1999;). The idea of applying the tensegrity model to cell and tissue architecture was initially proposed about 20 years ago by Ingber *et al*. (1981) and Ingber and Jamieson (1985). The tensegrity model states that cells, tissues and biological structures at smaller and larger size scales, all gain their shape stability, their ability to adapt their geometry and to maintain integrated mechanical behaviour through principles of minimizing the energy consumption. The term "tensegrity", a contraction of "tensional integrity", was created by Fuller (1975) as he explored a new architectural concept for building (geodesic domes, roofs) in which weight is minimized by separating compression members from tension members (Fuller and Marks, 1973). Note that, according to the definition given by Fuller, tensegrity structures fundamentally require a continuous tensional system associated with a discontinuous compression system, meaning that materialized bars and cables are not necessary, as far as continuous-tension is equilibrated by local-compression (Pugh, 1976). Applying this concept to the cell, Ingber *et al.* (1994) and Ingber (1997) consider that, in addition to (or in place of) intracellular elements given to support compression, e.g., the microtubules in conjunction with intermediate filaments or even a relatively rigid nucleus, some extracellular elements such as the non flexible extracellular matrix may support compression. The latter is the result of internal tension (pre-existing tension) generated actively in the cell's actomyosin-based contractile apparatus or passively by distension of actin filament due to external forces applied through extracellular adhesions.

Demonstrating that a given biological system follows the tensegrity principle remains a difficult task, hence the cellular tensegrity model has remained controversial (Ingber, 2000). Using traction force microscopy, Wang *et al.* (2001) have recently

solved one of the most critical assumptions about tensegrity (Heidemann *et al*., 1999; Ingber, 2000), i.e., that microtubules bear compression and are thus responsible for a significant portion of cellular prestress. Careful subcellular measurements of cytoskeletal mechanical response show that cellular models with more than one viscoelastic component are needed secondarily to the heterogeneous nature of the cellular components (Mathur *et al*., 2000; Yamada *et al*., 2000). Considering the cell as a hierarchical and multimodular structure with load bearing elements non infinitesimally small, i.e., as a non continuum model (Ingber, 1993; Chen and Ingber, 1999), it appears that improved cellular models must include an elastic submembranous cytoskeleton surrounding an internal tensed lattice of polymeric filaments (Ingber, 2000). Note, however, that the mechanical relevance of these two subcellular CSK components, whose microstructures are most likely organized at very different subcellular scales, has never been described.

The present study aims to evaluate the applicability and relevance of the tensegrity concept for the two individualized CSK networks which are known to play a specific role in the cellular response: (i) the cortical CSK connected to the inner face of the membrane which is composed of short actin filaments which forms a thin mantle investing the whole cell (Hartwig and Shevlin, 1986; Albrecht-Buehler, 1987; Cheng *et al*., 2000); and (ii) the inner cytosolic CSK component which links large regions of the cytoplasm through cross-linked networks of biopolymers (bundles of F-actin/microtubule/intermediate filaments).

2. METHODS

Tensegrity model (see Appendix)

The tensegrity structures tested here, i.e., a 16-element "cubic" model shown in Figure1A, and a 30-element "octaedric" model shown in Figure 1B, are respectively composed of four and six rigid bars, respectively compressed by a continuous network of $N = 12$ and $N = 24$ elastic pre-stretched cables. These two structures have been used to evaluate the effect of changing the number of constitutive elastic elements, i.e., $N = 12$ and 24. These two models have been separately studied in previous papers, i.e., Wendling *et al*. (2000a) for the 16-element model and Wendling *et al*. (1999, 2000b) for the 30-element model. In the Appendix, we present a short summary of assumptions, boundary conditions and a mathematical derivation of force equilibrium equations, leading to the determination of the main parameters governing the apparent elasticity modulus of these two tensegrity structures. For the 16-element model, an analytical solution may be obtained (Wendling *et al*., 2000a) while a numerical solution with a linear incremental method is required for the 30-element model (Wendling *et al*., 1999). We have modified the numerical solution obtained for the 30-element model to vary the conditions of attachment previously studied and to have the same number of "dependent" or fixed nodes in the two models, i.e., four nodes. The reason is that the global elasticity modulus has been shown to depend on both loading and attachment conditions as previously reported by Wendling *et al*. (2000b). More particularly, the elastic modulus was recently found (Cañadas *et al*., 2002) to differ by one order of magnitude when the forces were applied in the direction of bars of a 30-element tensegrity model and four fixed bottom nodes (#1, #2, #4, #8, see Figure 1B)

instead of applying forces with a 45°-angle from bar direction and three fixed nodes as in Wendling *et al*. (2000b).

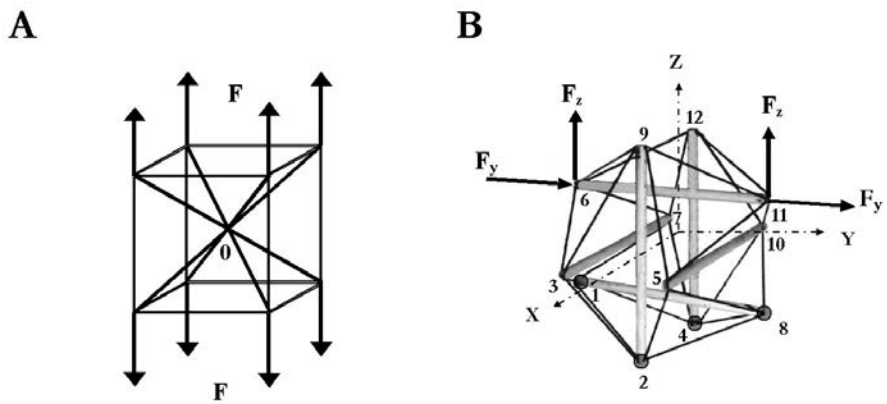

Figure 1. The two tensegrity models studied: (A) the 16 element model including $N = 12$ elastic elements compressing four rigid bars, and (B) the 30 element model including $N = 24$ elastic elements compressing six rigid bars. For the 30 element model, axial (z axis) and tangential (y axis) forces are applied on the upper bar at nodes {#6, #11}, while only extension and compression forces (z axis) are applied to the four upper and lower nodes of the 16 element model.

The governing parameters are the following non-dimensional quantities issued from equilibrium equations (exponent "r" refers to reference state):

$$T^* = \frac{T_c^r}{(ES)_c} \tag{1}$$

$$L^* = \frac{l_b^r}{r_b} \tag{2}$$

$$E^* = \frac{E}{E_c}. \tag{3}$$

The normalized elastic tension T^*, which actually corresponds to the initial strain of cables at the reference state ε_c^r, quantifies the basal level of internal tension (prestress) in the tensegrity structure. The normalized length L^* defines the characteristic scale of the overall tensegrity structure: the smaller L^*, the smaller the size of the structure and the smaller the free space volume between the constitutive elements (r_b is the bar radius). The apparent elasticity modulus E^* of the 30-element tensegrity model, normalized using the mechanical properties of cables, depends on L^*, T^*, N as well as attachment conditions, as explained above. Because boundary conditions (more specifically attachment and loading) determine degrees of freedom of each constitutive element, they will affect the absolute value of E^* for a given

structure. For the 16-element tensegrity model, the following analytical relationship can be obtained between E^*, L^* and θ, the angular position of the bar equals θ_{eq} at reference state, i.e., before applying external force:

$$E^* = \frac{\pi}{L^{*2}} \frac{F^*}{\sqrt{2}\left(\sin\theta - \sin\theta_{eq}\right)} \tag{4}$$

which obviously does not depend on T^*. This is probably because the directions of tensions in cables always form $\pi/2$ angles, hence a self-equilibrium exists between tensions in cables at each θ position and for small deformation of the tensegrity structure. Numerical solutions of Equation (A1) in the Appendix using incremental method has revealed the T^*-dependence of the structural stiffness E^* in the more general cases such as in the 30-element model.

Experimental Methods

A549 alveolar epithelial cell culture

A549 human alveolar epithelial cells (American Type Culture Collection, Rockville, MD) were grown to confluence in Dulbecco Modified Eagle Medium (DMEM) containing 10% of Fetal Bovin Serum (FBS), 2 mM L-glutamine, 50 IU/ml penicillin, 50 µg/ml streptomycin, and incubated in a 5% CO_2, 95% air atmosphere. Routine subcultures (passages 89 to 92) were performed at 1/20 split ratios by incubation with 0.025 g/100 ml trypsin-0.02 g/100 ml EDTA in calcium and magnesium free Phosphate-Buffered Saline (PBS) for 10 min at 37°C.

For magnetic twisting cytometry experiments, 96-well bacteriological dishes were coated with either fibronectin or type I collagen at a concentration of 5 µg/cm^2 for three hours at room temperature. Cells were plated at the density of 50×10^3 per well in complete medium with serum 24 hours before experiments, and incubated in serum-free medium with 1% of BSA 30 minutes before magnetic twisting cytometry experiments.

The Magnetic Twisting Cytometry (MTC) Technique

The CSK mechanical response of adherent epithelial cells was assessed by MTC using a laboratory made device, whose principle is similar to the one originally described by Wang *et al.* (1993). Carboxyl ferromagnetic beads (4.0-4.5 µm diameter, Spherotec Inc., IL USA) were coated with arginine-glycine-aspartic acid (RGD) peptide according to the company's procedure (Telios Pharmaceuticals Inc., CA USA) and bound to integrin transmembrane mechanoreceptors during the 20-min incubation time. Unbound beads were washed away with serum-free medium. Microbeads were then magnetized using a short uniform magnetic pulse (0.15 T during 150 µs). This magnetic field is horizontal, i.e., parallel to the monolayer of adherent cells. A magnetic torque was then created by Helmholtz coils, which generates a vertical uniform magnetic field at an intensity much lower than magnetization field ($B_{tw} \le 6.3$ mT). This magnetic torque T_{mag}, which is equal to the product of the magnetic moment of the bead **m** and the applied field $\boldsymbol{B}_{tw}$, induces bead rotation. The

calibration method used to estimate m (= 2.3 10^{-13} Am^2 in the beads used) is described in Laurent *et al.* (2002). By varying the intensity of the current (up to 15 A) in Helmholtz coils, $\boldsymbol{B_{tw}}$ could be modified, allowing application of a controlled mechanical torque for about one minute. The magnetic torque given by $T_{mag.} = \mu_0\, m\, H \sin\left(\frac{\pi}{2} - \theta(t)\right)$ with μ_0 being the permeability of the free space, slightly decreases as $\theta(t)$ increases. Using linear elasticity theory, Laurent *et al.* (2002) have described the effect of the partial bead immersion in the cytoplasm on Young modulus measurement $E\ (= \sigma/\theta)$. The applied stress was given by a formula $\sigma\left[= T_{mag}/(V \cdot \sin^3 \alpha)\right]$, which depends on the bead volume V and on the half-angle of bead immersion $\alpha = 67°$. The latter value has been previously estimated on a sample of beads in the same type of epithelial cells (Laurent *et al*., 2002). The bead deviation $\theta(t)$ which reflects the CSK time response to mechanical stresses, was measured by an on-line magnetometer which continuously detected the component of the remanent magnetic field $B(t)$ in the horizontal plane with a magnetometer of sensitivity of 0.14 nT using the formula: $\theta(t) = \cos^{-1}(B(t)/B_0)$, where B_0 is the mean value of the initial remanent magnetic field of the beads, i.e., before bead twisting. This method which actually measures the average projection $<\cos\theta(t)> = B(t)/B_0$, leads to a systematic overestimation of the average rotation angle because $\cos^{-1}(<\cos\theta(t)>)$ is always greater than $<\theta(t)>$, as shown by Fabry *et al.* (1999). It was assumed that the average bead deviation could be approximated by the arc-cosine of the projected magnetic field averaged over all beads (~ 200,000).

Analysis of CSK response by the two component model

The time course of this angular deviation during loading was analysed by a viscoelastic two-component "solid" model which can be seen as an equivalent model reflecting a variety of bead/cell/matrix attachment conditions. We initially verified (data not presented) that "fluid" models such as the Maxwell model or even a Kelvin (or a Voigt) model in series with a dashpot (Bausch *et al*., 1998, 2001), did not provide a satisfactory curve fitting of the "$\theta(t)$-plateau" shown in Figure 3B. The proposed two-component "solid" model consists of a series of two Voigt bodies representing the basic viscoelastic properties of the two CSK components (see rheological models in Figure 3B) instead of one as initially proposed (Wang *et al*., 1993). The choice of representing the two CSK components in series was guided by the best possible curve fitting and the observation that the local actin CSK was both surrounding the bead and connected to the more polymerised CSK filaments (see Results). Then, the time course of bead deviation $\theta(t)$ obtained during MTC was considered to fit the following equation (creep function):

$$\theta(t) = \theta_1(t) + \theta_2(t) = \frac{\sigma}{E_1}\left(1 - e^{-t/\tau_2}\right) + \frac{\sigma}{E_2}\left(1 - e^{-t/\tau_2}\right) \qquad (5)$$

and the time constants τ_1 and τ_2 are given by:

$$\tau_1 = \frac{\eta_1}{E_1} \quad (6)$$

and

$$\tau_2 = \frac{\eta_2}{E_2} \quad (7)$$

where E_1 and E_2 are the spring constants and η_1 and η_2 are the viscosities of the two components, respectively. To perform a rough evaluation of the prestress in each CSK component, we measured the mechanical response of living cells treated or not treated with low concentrations of cytochalasin D (1 µg/ml) and calculated the difference between CSK stiffness before and during cytochalasin D treatment as an index of the prestress. This method has already been used in previous studies to estimate the cellular tone (Pourati *et al*., 1998; Planus *et al*., 1999).

Visualization of the two CSK components

F-actin was stained with fluorescent phallotoxin. Small plastic wells were fixed with silicone on round glass coverslides which were placed in Petri dishes and the inside surface of the wells (0.5 cm^2) was coated with fibronectin at a concentration of 5 µg/cm^2. Cell monolayers were rinsed twice with warm CSK-buffer (25 mM HEPES, 2mM $MgCl_2$, 30 mM MES, 10 mM EGTA, 300mM sucrose, pH 6.9) in order to maintain CSK integrity, as previously described. Cells were then fixed in 1% glutaraldehyde in CSK buffer for 15 minutes and incubated for two more minutes with 0.5% Triton X100 and 0.25% glutaraldehyde in CSK-buffer at 37°C. The samples were rinsed twice with CSK-buffer. Rhodamine phalloidin (0.76 µM) was dissolved in CSK-buffer and added to each sample for 30 minutes in the dark and under humid chamber at room temperature. Coverslides were rinsed twice for five minutes with CSK-buffer, then a final rinse was performed with ddH_20. The coverslides were mounted with 100 µl of mounting medium on top of the cell monolayer to keep the cell thickness intact. Samples were stored overnight at 4°C before examination by laser confocal microscope.

Stained cell monolayers were observed using a LSM 410 invert confocal microscope (Zeiss, Rueil-Malmaison, France). The latter has two internal helium-neon lasers and one external argon ion laser. Image processing was performed using LSM 410 software. Fields of cells were randomly selected, brought into focus using a ×63/1.4 numeric aperture Plan Neofluor objective. Epifluorescence was detected for 488nm excitation and 515-520nm emission (green) and 543 nm excitation and 570 nm emission (red). A cross sectional image was recorded under confocal conditions and used to establish a plane of focus above the glass surface. Optical sections were recorded every 1µm to reveal intracellular fluorescence. Apical localization of labelling was determined by obtaining vertical section.

To undo the distortion due to the optical system of the confocal microscope, a 3D-deconvolution process was performed on the stack of grey level images (8 bits) by the appropriate software's module AxioVision 3.0.6 (Carl Zeiss, NY USA). The deconvolution process uses a mathematical algorithm which takes into account the theoretical function PSF (Point Spread Function) calculated for each of the acquisition

parameters. The fixed images data are implemented at the right scale in Amira 3.2 software (TGS Inc., CA USA) which uses the threshold segmentation method to extract cell contours. Contours of external and internal subcellular structures corresponding to different levels of fluorescent intensity where defined using the curve of the "logarithmic" decrease in cumulated pixels of the stack images versus the grey level (0 to 255). The 3D-reconstruction was performed by a GMC module (Generalized Marching Cube algorithm) of Amira software which generates, using a triangulation method, an isosurface from segmented optical planes. Visualization of the 3D-reconstructed cells was performed using 3D-Studio Max v3.1 software (Kinetix, CA USA), allowing calculation of volume from a surface, permitting by Boolean operations to generate vertical sections in the 3D-reconstructed cell.

3. RESULTS

3D-reconstruction of the cortical and cytosolic CSK

Figure 2A presents an image of the spatial distribution of actin filaments in a fixed alveolar epithelial adherent cell obtained by confocal microscopy. Actin filaments, stained with fluorescent phallotoxin, are colored differently according to their height in the cell. This non confluent flattened cell seems highly attached to the substrate and thus highly tensed. Bundles of actin filament (stress fibers) essentially visible in the basal plane (see Figure 2B) cross the entire cell, linking large portions of the cytoplasm and even opposite sides of the cell. These F-actin "macro" structures are organized in various directions throughout the cell, predominantly along the longitudinal axis and the transversal axis, thus forming almost right angles. Although non-actinic biopolymers which compose the CSK are not visible in Figure 2, they could play a role such as counterbalancing tension generated in these cell-size scale organized stress fibers. Note that curvature of many stress fibers located on the cellular periphery strongly suggests the role of internal tension radially directed towards the inner cell. The optical planes shown in Figure 2A as well as the 3D-reconstructions of the actin filament structure shown in Figures 2 B-D support some of the above assumptions as well as some of the model assumptions. Figure 2B is a view of the actin network from the bottom showing that the cell is attached to the substrate through a peripheral zone of adherence whereas transversal stress fibers or actin bundles organized in the lower plane, constitute the lower, almost individualized CSK actin structure, near the basal plane (see the diagonal cross-section in Figure 2D). These actin bundles which are organized at a scale close to the cell size and over large distances between adhesion points, mainly represent the tensile elements of the cytosolic CSK. The actin structure of the cytosolic CSK may also be seen from the dense and highly polymerized actin CSK shown (in dark blue) in Figure 2C and Figure 2D while the cortical CSK structure is visible in the same figures (in transparent light blue). Figures 2C and 2D show that a thin network of low actin density surrounds the entire cell, except may be near the basal plane, in this studied cell. It is noteworthy that the bead appears partially embedded in this cortical low density actin CSK network as shown in Figure 2D. Moreover, the cortical CSK dome appears tensed probably because load bearing elements are able to support tension, e.g., the rigid nucleus (presently not marked) or the dense actin filaments which appear

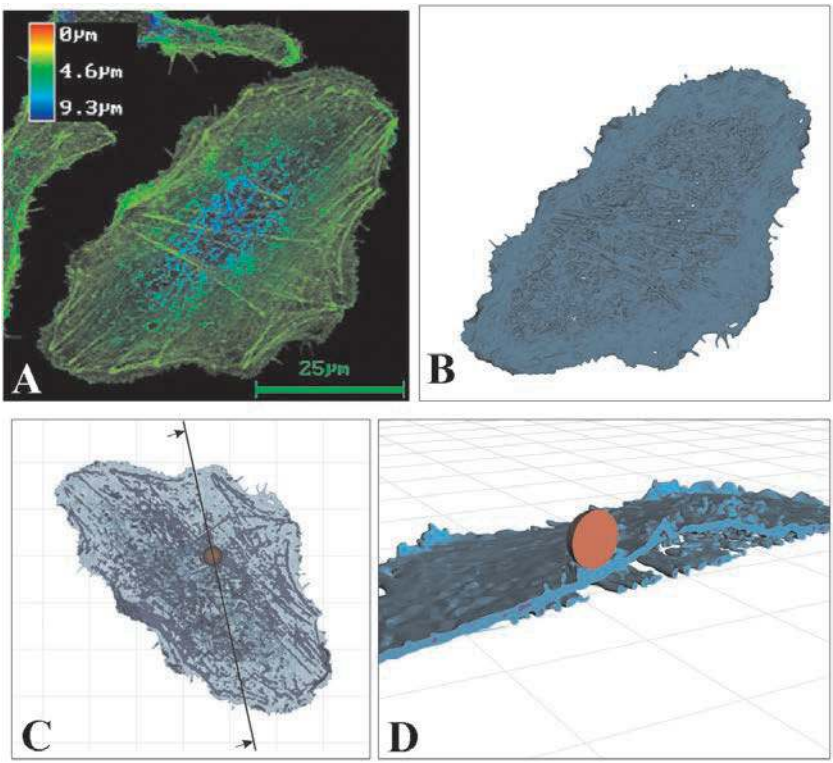

Figure 2. (A) Views by confocal microscopy of actin filaments stained by fluorescent phallotoxine in an adherent epithelial cell, (B) Basal face of the 3D reconstruction of the actin cytoskeleton viewed from below, (C) Apical face of the 3D reconstructions with two levels of fluorescent intensity given to represent the cortical (transparent blue) and the cytosolic (dark blue) CSK components, (D) Cross sectional view of the two cellular actin CSK networks and the bead CSK interaction according to the bead axis shown in (C).

from place to place on the apical face in the "cortical" CSK while it constitutes most of the "cytosolic" CSK on the basal face. By contrast, most of the high density actin CSK network, which appears as an underlying scaffold organized essentially near the basement substrate and clearly below the bead, does not seem to be directly attached to the bead surface in this cell. As a matter of fact, the high density actin structure is always embedded in a surrounding low density actin structure whose thickness varies, depending on the cellular position. Although the bead surface was not specifically marked in these experiments, it was possible to spatially reconstruct the bead position in the cell (see Figures 2B and 2D) using spheres whose sizes and location in the cortical CSK were precisely determined, either under direct confocal microscopy or during post-acquisition from cell images stored in Interferential Contrast Nomarski. Figure 2D confirms that the degree of bead immersion in the cellular medium could also be determined by generating vertical sections with the reconstruction program (see also Laurent *et al*., 2002). This allows improvement of the calibration of the

experimental method. On the whole, from the reconstructed images of the studied epithelial cells, we consider that the thin mantle of actin CSK which determines the external structure and the shape of the cell mainly represents the "cortical" CSK component with however a few embedded fibres of dense actin (Figure 2D). The characteristic length of the meshwork which composes the cortical CSK structure is probably too small to be visible on the confocal images of Figure 2. By contrast, the cytosolic CSK is essentially composed of dense actin fibres or bundles of actin filament. It will be assumed that the cortex of low density actin filaments which coaxially surrounds dense actin fibres (see bottom fibres in Figure 2D), does not predominate in the mechanical response of the stress fibre.

Mechanical response of the partitioned CSK

A typical CSK response obtained with MTC is shown in Figure 3A as a function of bead rotation angle $\theta(t)$ versus time. There are two phases: period I which precedes bead rotation and which corresponds to the bead position before stress, i.e., $\theta(t) = 0°$ obtained for $B(t) = B_0$, and period II during which the application of the magnetic torque T_{mag} results in a rapid increase in bead deviation to reach a plateau within a minute of torque application. A transient stress (up to 23 Pa in the case of Figure 3) is applied and the solution resembles a creep function except that amplitude of the stress (ratio of torque to bead volume) is decreased by a factor $\cos\theta(t)$. Because a plateau is reached (within a minute), the response is typical of a viscoelastic solid and resembles responses previously measured (Wang *et al*., 1993). In Figure 3B, the experimental curve response is fitted by a viscoelastic "solid" model: the simple Voigt model ($\tau = 1.4$ s, $E = 65$ Pa , $R^2 = 0.70$), classically used in previous MTC studies (Wang *et al*., 1993; Pourati *et al*., 1998; Planus *et al*., 1999). This classical model is compared with the proposed double Voigt model which partitions the CSK into two components ($\tau_1 = 0.9$ s, $E_1 = 68$ Pa and $\tau_2 = 28$ s, $E_2 = 229$ Pa, $R^2 = 0.88$). Clearly, during the minute of stress applied, the proposed two-component model provides a much more satisfactory curve fitting than the classical single Voigt model (Figure 3B). Since the time constant τ_1 and τ_2 differed by more than one order of magnitude for the four levels of stress applied (see Figure 4A), we have attributed the mechanical properties of the fastest components to the cortical CSK component since it is immediately sensed by the bead (Figure 2D) and the properties of the slowest component to the deep CSK component (Figures 2C-2D). Stiffness of the cortical and cytosolic CSK networks are plotted in Figure 4B for four predetermined values of applied stress, i.e., σ_0 (= torque/0.78 x bead volume) = 13, 23, 31 and 38 Pa, which resulted in values of bead deviation angle (θ_{max}) from 21° (at $\sigma = 13$ Pa) to 32° (at $\sigma = 38$ Pa). Mean values of CSK stiffness were significantly higher for the cytosolic CSK (E_2 = 95-204 Pa) than for the cortical CSK (E_1 = 63-109 Pa) at each level of stress applied (Figure 4B). Moreover, the studied cells express a stress-hardening response more marked for the cytosolic CSK than for the cortical CSK (Figure 4B). Prestress of the cortical and the cytosolic CSK was estimated from the contribution of the F-actin network to the rigidity. Previous studies have shown that actin filaments provided the highest contribution to cellular rigidity and that depolymerization of F-actin by cytochalasin D

tended to remove (Wang, 1998) or at least reduce (Wendling *et al.*, 2000b) the internal tension in the cell. We have defined the prestress-related rigidity ΔE (basically ΔE_1 for the cortical and ΔE_2 for the cytosolic) as the difference in rigidity values measured before and during cytochalasin D treatment, e.g., $\Delta E = E_{\text{without cyto D}} - E_{\text{with cyto D}}$. The two CSK components exhibit significant differences in ΔE with values of prestress-related rigidity higher for the cytosolic than for the cortical CSK, i.e., $\Delta E_1 < \Delta E_2$ (see Figure 4C).

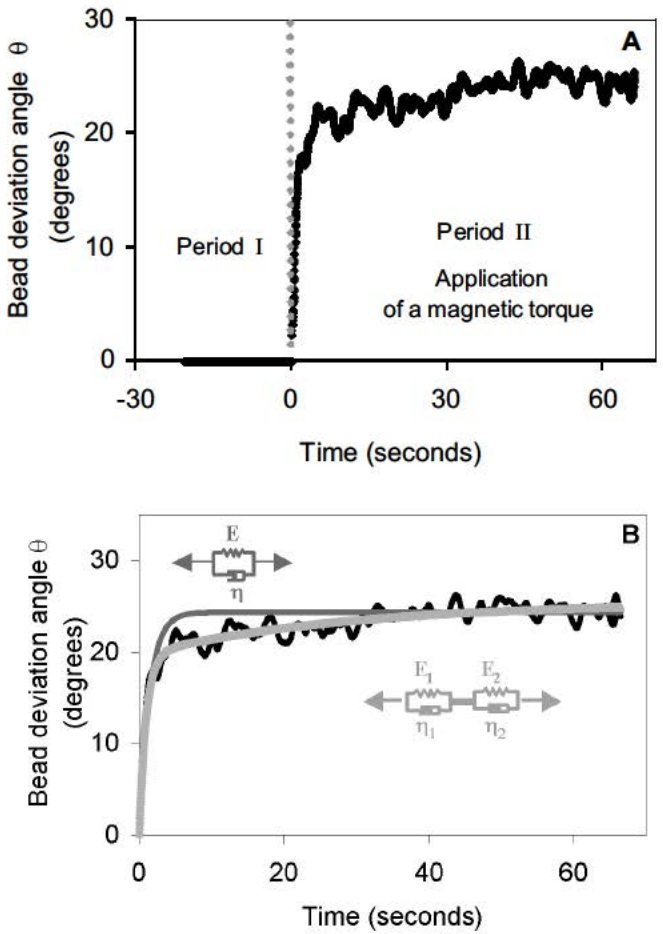

Figure 3. (A) A typical signal of bead deviation angle obtained with Magnetic Twisting Cyto metry, Period I: before applica tion of a magnetic torque, Period II: during application of magnetic torque (23 Pa), and (B) adjustment with simple Voigt ($R^2 = 0.7$) and double Voigt ($R^2 \approx 0.9$) models. The simple Voigt is the standard model proposed in initial studies (Wang *et al.*, 1993; Wang and Ingber 1994). The proposed double Voigt model provides the viscoelastic properties of the cortical and cytosolic CSK components

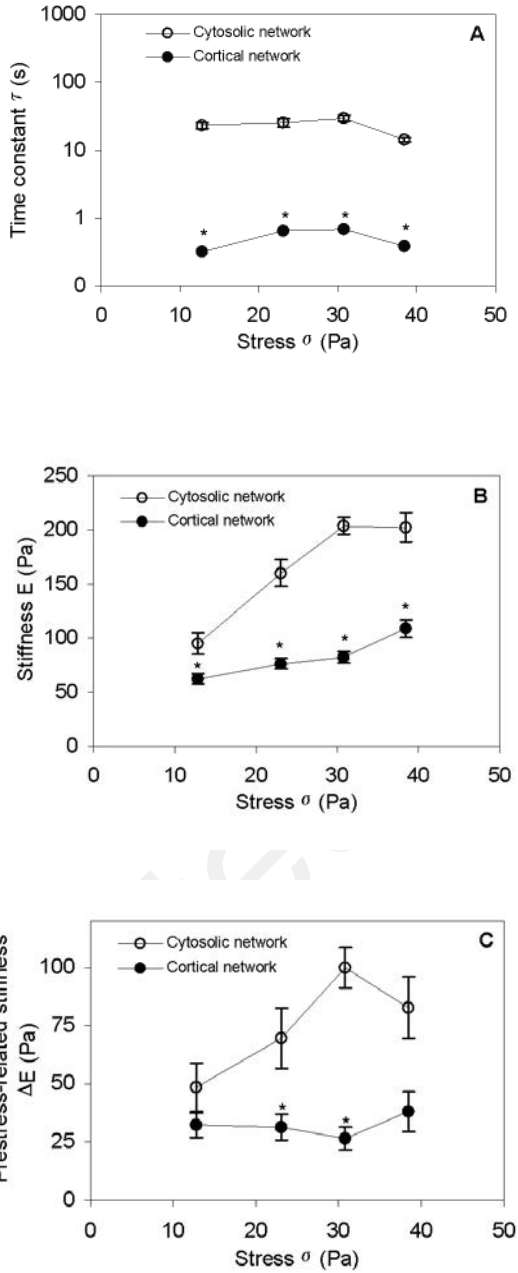

Figure 4. Experimental results obtained in living adherent epithelial cells with Magnetic Twisting Cytometry for four different values of applied stress, i.e., 13, 23, 31 and 38 Pa. (A): Plot of the viscoelastic time constant (in s) of the cortical and cytosolic CSK components; (B) Plot of the stiffness (Young elasticity modulus in Pa) of the cortical and cyto solic CSK compo nents; (C) Plot of the prestress related stiff ness (ΔE in Pa) for the cortical and cytosolic CSK com ponents, estimated from the F actin contribution to stiff ness, i.e., the difference between stiffness values before and during F actin depolymeriz ation by adding cytochalasin D. Values are mean ± SD and $n = 8$ wells for each point. $^*p < 0.05$, means a significant difference.

Normalized laws of structural stiffness for tensegrity structures

The force-displacement relationship of tensegrity structures, although composed of linear elastic elements, was previously found to be non-linear, due to the contribution of the spatial organisation of constitutive elements. Hence, the proposed concept of structural stiffness that we presently attempt to quantify. Accordingly, the stress-strain relationships is also markedly non-linear for both models tested, the smaller L^*, the stronger the σ–ε non-linearity (results presented in Wendling *et al*. (1999, 2000b). In addition, the 30-element model (with the four lower nodes fixed) reveals a T^*-dependency such that, the higher the value of internal tension T^*, the more marked the non-linearity. This non-linear stress-strain behaviour corresponded to a linear strain-hardening response in traction and compression, while, in shear, the structural response was a transition between these two behaviours, depending on specific strain value ($\varepsilon = 0.2$ with four attached nodes (Cañadas *et al*., 2002), and $\varepsilon = 0.5$ with three attached nodes (Wendling *et al*., 1999)). The elasticity modulus at zero strain E^* (structural stiffness) differed from zero and exhibited a marked dependence on L^* and a less marked dependence on the value of cable prestress T^*. It is noteworthy that the slopes of the relationships between E^* and L^* are similar for the 30-element and the 16-element models, i.e., E^* is proportional to $1/(L^*)^{-2}$ (as shown in Figure 5 and, for the 16-element model, in the explicit form of Equation 7), as already reported by Wendling *et al*. (1999), Wendling *et al*. (2000ab) and Cañadas *et al*. (2002). Attachment through four nodes instead of three resulted in no change in L^*-dependence of E^* even though E^*-values were one order of magnitude higher when the number of fixed nodes was increased. By contrast, the T^*-dependence of E^* was much less marked and seemed affected by a number of factors such as the number of bars and the attachment conditions. The E^*-T^* relationships obtained for the different models are presented in Figure 6. The structural stiffness of the 16-element model does not depend on T^*. The structural stiffness of the 30-element model was slightly dependent on T^*, depending on the type of loading and the range of T^*, i.e., $(T^*)^{0.3}$ in extension and $(T^*)^{0.7}$ in shear and $T^* = \{0.25\text{-}1\}$ (four lower nodes attached) and $(T^*)^{0.5}$ in extension and compression and $T^* = \{10^{-3}\text{-}10^{-1}\}$ (three lower nodes attached (Wendling *et al*., 2000b)). The N-dependence of the structural stiffness E^* (N: number of elastic elements) was extrapolated in Figure 7 from the results obtained in the two studied tensegrity models and at the same L^*. The slope of the E^*-N relationship appears close to "–3.5" on the double logarithmic scale in Figure 7, i.e., the E^*-N was largely non-linear, even more than the E^*-L^* relationship. Although extrapolated from two relatively close tensegrity models in terms of element number, these results are consistent with the theoretical background synthesized by Pugh (1976). Indeed, this author has stated earlier that cylindrical tensegrity structures, which are basically composed of multiple layers of repetitive bar-cable assemblies, become weaker and even lose their stability when increasing the number of bars per layer. Altogether, these results mean that, at given values of L^* and T^*, the structural stiffness E^* decreases as the number of constitutive elements of the tensegrity structure increases.

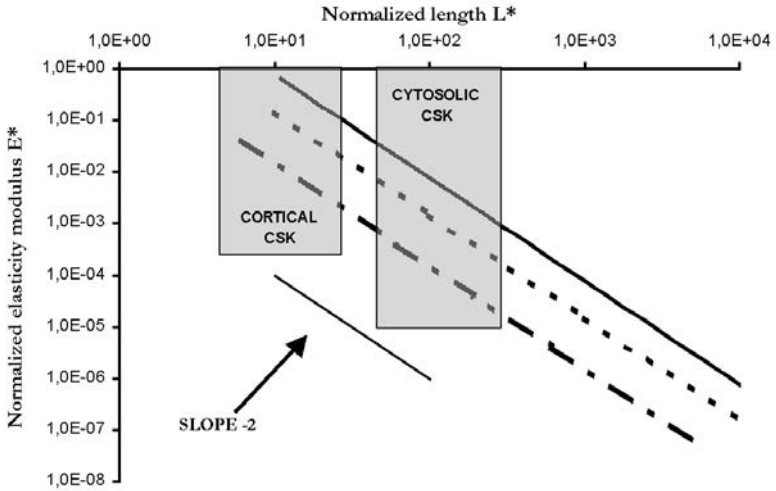

Figure 5. Theoretical results obtained by numerical simulation in the 16 element model (continuous line) and the 30 element model (dotted line for four lower attached nodes; dash dotted line for three lower attached nodes). *E** (normalized elasticity modulus) is plotted versus *L** (normalized length). Shaded areas give the presumed ranges of *L** for cortical and cystosolic CSK components.

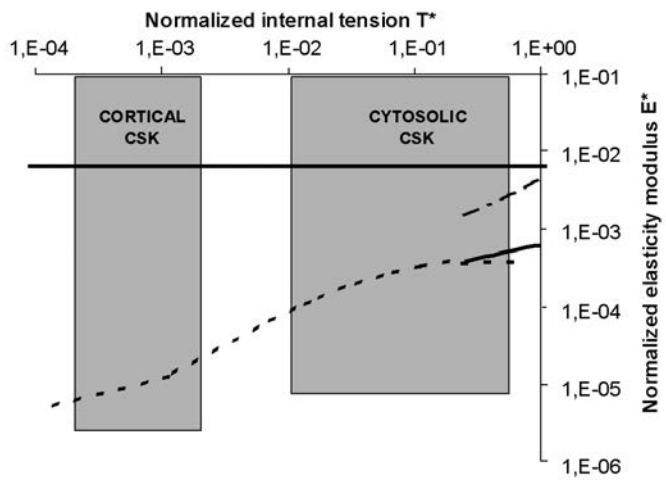

Figure 6. Theoretical results obtained by numerical simulation in the 16 element model (continuous horizontal dark line) and the 30 element model (dotted line for extension and four lower attached nodes; dash dotted line for compression and extension for the three lower attached nodes; grey continuous line for shear and four lower attached nodes). *E** (normalized elasticity modulus) is plotted versus *T** (internal tension or initial strain in elastic elements). Shaded areas give the presumed ranges of *T** for cortical and cystosolic CSK components.

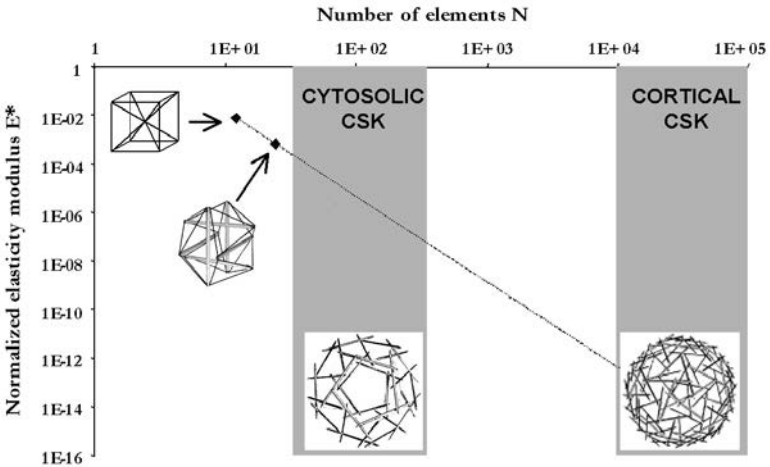

Figure 7. Extrapolated relationship between E^* (normalized elasticity modulus) and N (number of elastic elements) obtained from the two tensegrity models studied ($N = 12$ for the 16 element model, and $N = 24$ for the 30 element model). Shaded areas give the presumed ranges of N and E^* for the cortical and cytosolic CSK components.

4. DISCUSSION

From the bead twisting measurements in living adherent cells we demonstrate that the cytoskeleton response may be advantageously partitioned into a slightly tensed, easily deformable cortical CSK component and a highly tensed and largely rigid 3D-internal cytosolic CSK network. In addition to the significant level prestress presently attested by the non zero values of prestress-related rigidity (shown in Figure 4C) or by the non zero value of stiffness extrapolated at zero stress (in Figure 4B), the two CSK components, and more particularly the cytosolic one, exhibit very different time constants for their viscoelastic response (shown in Figure 4A) and a specific stress-hardening response (shown in Figure 4B). In early experimental studies in living cells (Wang *et al*., 1993; Wang and Ingber, 1994), confirmed by theoretical studies on tensegrity models (Stamenovic *et al*., 1996; Stamenovic and Coughlin, 1999, 2000; Wendling *et al*., 1999, 2000b), prestress and stress-hardening responses were given to characterize tensegrity behaviour. These two mechanical features will be found in the two CSK components constitute similar arguments to conclude that the two CSK components have a tensegrity behaviour as far as we are able to relate above results to specific geometrical and mechanical properties of elements constituting each microstructure (see Tensegrity Model). This point is considered in detail below.

Mechanical and structural relevance of CSK partitioning

Because the two CSK components have quite a different time response and significantly differ in terms of stiffness and prestress, the pertinent parameters characterizing the microstructures of each component should differ greatly. From

reconstructions of 3D-actin structures obtained at the lowest density F-actin structure and at a rather high density F-actin structure, it appears that the structures corresponding to these two levels of F-actin density have quite a different shape and organization. Consistently with its functional role which is to be involved in rapidly changing interactions at the cell-ECM interface, we assumed that the cortical CSK is the faster and softer CSK component and would predominantly contain a high number of slightly-dense and short actin filaments. In contrast, the cytosolic CSK which ensures cellular stability and anchorage of the cell to the substratum through focal adhesion is the slower and stiffer CSK component would predominantly contain a smaller number of highly-dense and long F-actin fibers (Choquet *et al*., 1997). Theoretical results on tensegrity structure suggest that the cortical and the cytosolic CSK could be seen as two different forms of tensegrity structures, assembled from the constant amount of available actin (F or G) in a given cell. Pugh (1976) has shown that different families of polygonal forms can be obtained by changing the number of constitutive elements and their length. More specifically, open space may develop at the center of a polyhedric structure leading to geodesic domes when the number of elements increases (Pugh, 1976). Such an evolution is observable in the two simplified tensegrity models tested as the number of elastic elements is only doubled. Thus the cytosolic and cortical CSK microstructures might indeed obey the same tensegrity concept, except that their form and thus mechanical properties, correspond to quite a different number of filaments, probably in relation to their difference in functionality.

The cortical cytoskeleton determines membrane topology and is intimately involved in "plasma membrane"-associated cellular functions (Bretscher, 1991; Hamill and Martinac, 2001). 3D-reconstructions of the low density actin filament network performed in this study revealed that cortical actin constitutes a thin mantle everywhere in the cell, almost continuously on the apical face. The other CSK component is the internal cytosolic CSK which acts globally and thus ensures stabilization and coordination between the parts and the whole cell (Ingber, 1993, 1997; Ingber *et al*., 1994). 3D-reconstructions of the high density actin filament network in a highly spread cell (Figure 2) revealed that the cytosolic actin network is predominantly organized near the basal face, with bundles of actin filaments approaching the cell size. Mechanical behaviours determined by the proposed analysis demonstrate that the cortical and the cytosolic CSK components have quite a different time response while they both exhibit an almost linear stiffening response to stress, which is consistent with the tensegrity model behaviour shown in previous papers (Wang *et al*., 1993; Wang and Ingber, 1994; Wendling *et al*., 1999; Wendling *et al*., 2000b). In addition, the less marked stress-dependency observed for the cortical CSK component (Figure 4B) suggests that values of governing parameters, i.e., characteristic length, internal tension, number of elements, may all greatly differ between the cortical and the cytosolic CSK which is extensively discussed below. At last, the experimental estimate of the prestress in each component performed on the basis of the contribution of actin filaments to rigidity (see Figure 4C and Pourati *et al*., 1998; Planus *et al*., 1999) shows that the cortical CSK is much less tensed than the cytosolic CSK. Note that the tensegrity model predicts that the less prestressed structure, the smaller the stress hardening response. Such a property is observed when comparing the cortical to the cytosolic CSK behaviours, but it was previously observed when comparing cells depolymerised for actin after cytoD treatment to

untreated cells (Wendling *et al*., 2000b). Early studies by Wang *et al.* (1993) have emphasized that the linear stress hardening response observed both in the cytoskeleton of living adherent cells and in a weight-loaded geodesic array of wood dowels and elastic threads, was explained by their common tensegrity nature. Since this time, several theoretical studies including the present one, have been performed on the 30-element model (octahedron) (Stamenovic *et al*., 1996; Stamenovic and Coughlin, 1999, 2000; Wendling *et al*., 1999, 2000b) and have brought new knowledge on tensegrity structure and its possible biological relevance. Above all, the tensegrity concept allows understanding of how CSK substructures organized at various scales and/or at different locations in the cytoplasm, can have a specific contribution to cellular function.

Physical properties of cortical CSK structure

Characteristic length and number of elements

It is noteworthy that the cortical CSK can be evaluated because the bead acts as a local extracellular matrix for the cell, hence the possible recruitment of cortical actin filaments in the bead neighbourhood (as shown in Figure 2D). Unfortunately, the present definition of microscopic images does not allow the revelation of the details of the ultrastructure of the cortical actin in studied epithelial cells. We thus purposely used data published in the literature. For instance, the cortical actin network has been previously described for macrophages as a dense network of 10 nm-diameter filaments that invests the whole cell as a thin 200-500 nm-thick mantle similar to the one observable in Figure 2D (Hartwig and Shevlin, 1986). In that study, the spacing between filament ramifications was found to be of the order of 100 nm and at a density presently estimated from the reported image to a few hundred filaments per μm^2. Reconstruction of the cortical actin structure from stereo images has led to thickness values of 90 nm and an estimated average filament length of about 100 nm in endothelial cells (Cheng *et al*., 2000). It can be concluded that most of the eukariotic cells, including the epithelial cells tested, are encompassed within a cortical CSK structure made of actin filaments 100 per μm^2-dense, 100 nm long and around 10 nm width. Thus, the cortical CSK can be seen as a discrete geodesic structure whose characteristic length $L^*\left(=\dfrac{\text{actin filament length}}{\text{actin filament radius}}\right)$ might approach L^* = 5-50, number of actin filaments in the range: $N = 10^4$-10^5, estimated from the density of cortical actin filaments given in Cheng *et al*. (2000) and a cortical volume approximated from 3D reconstruction shown in Figure 2.

Note that actin filament organization and thus function and mechanical properties of the cortical CSK can be modulated by a number of factors such as acting binding proteins, angles between filaments (Hartwig and Shevlin, 1986; Wachsstock *et al*., 1994). Note also that in addition to actin binding proteins, myosin II is a molecular component of the cortical cytoskeleton which is presumed to act as small tension rods that "tighten up" the cortical actin cytoskeleton. Thus, even in non muscle cells, myosin II molecules are known to contribute to cortical CSK prestress, stabilization and stiffening of the plasma membrane, complementarily to actin filaments of the

cytosolic CSK (Lodish *et al.*, 1999). Note however that a flexible, yet strong, submenbranous lining or membrane CSK appears to be better suited to regulating the properties of plasma membrane than do actin filaments (Fox and Boyles, 1988).

Characteristic tension

Obtaining accurate values of cortical prestress, i.e., before any area expansion, remains a difficult task. Red cells have been evaluated by micropipette aspirations and cortical tension (at rest) has been estimated at the presumed equilibrium state (corresponding to the equivalence between the deformed cell length and the initial cell radius). These data have shown that the underlying cytoskeleton of the red cell membrane possesses a shear elasticity modulus in the range 6-9 pN/µm (Hochmuth and Waugh, 1987) which remained two to four times smaller than the value of the area expansion modulus (Discher *et al.*, 1994; Discher and Mohandas, 1996). In neutrophils, a typical value of cortical tension was $T_c = 24$ pN/µm when extrapolated before any area expansion (Needham and Hochmuth, 1992) or $T_c = 35$ pN/µm at the critical point of transition between elastic solid and fluid behaviour. Values of area expansion modulus for neutrophils were found to be similar to the values for red cells, e.g., 39 pN/µm, suggesting that a similar cytoskeletal network may exist at the inner surface of these highly deformable cells.

Extending to "solid" cells, the formula issued from continuum "fluid" models (i.e., Laplace's law), Hochmuth (2000) found values of cortical tension in chondrocytes and endothelial cells approximately 100 times greater, e.g., $T_c = 2200$ pN/µm. In the present bead twisting study, an estimate of the cortical tension, calculated from the formula given for "solid" cells (Equation 6 in (Hochmuth, 2000)), and using the prestress-related rigidity value given in Figure 4C (e.g., 25 Pa at $\sigma = 31$ Pa), as well as the bead radius, leads to $T_c = 125$ pN/µm, i.e., an equivalent cortical tension value which appears in between "soft" cells and "stiff" cells. Many factors could explain the discrepancies between values of cortical tension estimated in epithelial cells and those in endothelial cells or chondrocytes. One may mention: (i) different types of efforts between MTC and micropipette aspiration, (ii) different cellular remodeling process eventually in relation with different binding affinity (Sato *et al.*, 1987), (iii) the tendency of MTC technique to underestimate cellular stiffness and by extension the cortical and cytosolic stiffness. Concerning point (i), shear modulus instead of area modulus could contribute to the torsion imposed to the local cortical CSK during bead twisting, leading to values of T_c a few times smaller. Concerning point (ii), it is possible that receptors of epithelial A549 cells have lower affinity with fibronectin than endothelial cells, leading to smaller values of stiffness. Concerning point (iii), we provide an exhaustive discussion of the physical reasons behind the systematic underestimation with MTC in Laurent *et al.* (2002).

A straightforward but rough estimate of T^* for the cortical CSK structure can be estimated from Equation (4) using the prestress-related stiffness (shown in Figure 4C) assuming a ratio of cortical CSK deformation to actin filament strain in the range {1-10}:

$$T^* = (\Delta E.S.\varepsilon)_{\text{cortical CSK}}/(E.S.\varepsilon)_{\text{F-actin}} \sim 2.10^{-4}\text{-}2.10^{-3},$$

where $\Delta E_1 = 25$ Pa (at $\sigma = 31$ Pa) is the actin contribution to the stiffness of cortical CSK (Figure 4C), $E_{\text{F-actin}} = 2.6$ GPa, is the Young's modulus of isolated actin filament element given by Gittes *et al.* (1993) and $S_{\text{F-actin}}$ ($\approx 10^{-4}$ μm^2) is an estimate of the cross-sectional area of the filaments given above. Note that these values are consistent with those used in previous studies (Coughlin and Stamenovic, 1997; Wendling *et al.*, 2000b).

Physical properties of cytosolic CSK structure

In addition to the cortical CSK, most eukariotic cells and especially adherent cells have a three dimensional inner cytoskeleton in which assemblies of actin filaments such as stress fibers or bundles of actin filaments play a predominant role. Stress fibers are actomyosin-based CSK structures observed everywhere in the cytoplasm, which may link opposite faces of the cell membrane (Katoh *et al.*, 1995) and thereby pertain and interconnect the two CSK components. The 3D-reconstruction of the actin network shown in Figure 2 is particularly demonstrative of this point. It has been shown that stress fibers behave as truly contractile structures, even when separated from the contractile cell cortex, the cortical CSK, to which they are attached (Katoh *et al.*, 1998). The characteristic length of stress fibers has been given by Katoh *et al.* (1998) to be about 90±40 μm for a diameter of 0.1 μm, but values as low as 10μm could be observed as in Figure 2, leading to values of $L^*\left(=\dfrac{\text{actin fibre length}}{\text{actin fibre radius}}\right)$ in the range: L* = {100-1000}, i.e., one or two orders of magnitude above the L^*-values given for the cortical CSK structure. The number of actin filament assemblies in the cytosolic component can be estimated to be in the range N = 50-500 from Figure 2. Estimation of the contribution of actin to the rigidity (or prestress) of the cytosolic CSK component (from data in Figure 4C) leads to values about two or three times higher than the values obtained for the cortical CSK. These differences between the cortical to the cytosolic values should correspond to higher values of internal tension in the cytosolic CSK. However a straightforward application of formula used for the cortical CSK is suspicious because the basal state of the internal CSK is not known especially in these adherent cells. Indeed, in the spread cell shown in Figure 2, it is hard to estimate the internal tension because, due to attachment conditions, the cell is far from the basal state cell as it has to generate stabilization forces and tension using the contractile apparatus to equilibrate the compression through the quasi inflexible support. Otherwise, non adherent eukariotic cells chose a spherical configuration with almost no cytosolic CSK containing long stress fibers. Hence, estimation of T^* for the cytosolic CSK component requires assuming a value of initial strain for the stress fiber. The basic macromolecular assembly of the stress fiber seen as the prototype of striated muscle sarcomere is known to be able to elongate up to 80% (Fung, 1981). Although the exact prestress value of the cytosolic CSK is difficult to determine, it seems realistic to consider a relative high range of T^* values, i.e., T^* = {0.01–0.5} considering that actual attachment conditions largely contribute to raise the T^* value, by comparison to the resting conditions of a cytosolic CSK structure in a non attached cell which could not exist.

Comparison cortical vs cytosolic properties based on tensegrity model

Based on the above considerations, the range of L^*, T^* and N attributed to each CSK component is presented in Figures 5-7. Compared to the cytosolic range of L^* (= 10^2-10^3) and N (= 50-500), it appears that the smaller range of L^*-values (i.e., L^*= 5-50) estimated for the cortical CSK could not compensate the much higher number of elastic elements (i.e., $N = 10^4$-10^5), meaning that structural stiffness of cortical CSK would indeed be smaller than cytosolic CSK (see Figures 5 and 7) which is consistent with experimental results. Resulting effects on prestress predicted by E^*-T^* relationships given in Figure 6 indicates that the cortical stiffness would be smaller than the cytosolic stiffness which is also consistent with present experimental results. Note that differences in stiffness (or prestress-related stiffness) of less than one order of magnitude could correspond to prestress discrepancies of several orders of magnitude as predicted by the tensegrity models (Wendling *et al*., 1999, 2000b).

One of the major criticisms against the cellular tensegrity model is that a highly local response did not result in distributed, generalized changes in cell shape nor in filament array while the tensegrity model predicts an integrated and distributed response (Heidemann *et al*., 1999). These observations were given to contradict the tensegrity concept of global structural rearrangement of the cytoskeleton (Ingber, 2000). However, based on the present results, we believe that they may not precisely contradict tensegrity because the CSK does not have a unique response corresponding to a unique structural size scale, as presently demonstrated.

One of the future problems is to determine, for each cell type and undergoing function, the partition between (i) the cortical CSK whose geodesic organization at a subcellular level permits rapid adaptation and sensitivity to local mechanical changes, and (ii) the highly tensed cytosolic CSK whose spatial organization at large cellular size permits shape stability, resistance to deformation and maintenance of attachment to the base. However, we are aware that tensegrity models, even more complex than those studied, remain largely oversimplified compared to the biological reality. A number of factors such as the role of interdependency between internal tension and attachment of the cell to the base, the strength of molecular links and particularly between the two CSK components considered, the type of loading, the compressive role of nucleus due to higher stiffness (Mathur *et al*., 2000; Caille *et al*., 2002), the role of other polymeric networks and notably the compressive role of microtubules, the actomyosin and polymerization processes, are only partly or not at all taken into account by the present approach. Some of these factors have already been evoked in previous reviews (Thoumine, 1996; Ingber, 2000; Wang *et al*., 2001) but many of them require further studies. Despite the obvious oversimplification of biological reality brought by the present model, the present experiments performed in living adherent epithelial alveolar cells, provide a body of structural/mechanical/functional arguments to support the concept of partitioning the cytoskeleton into a 2D-cortical and a 3D-cytosolic CSK components. The present study brings arguments suggesting that the specific mechanical behaviour of each CSK component seems to be supported by the tensegrity concept. Indeed, mechanical property measurements could be correlated to the tensegral properties of the cortical and the cytosolic micro-structures i.e., normalized length (L^*), normalized tension (T^*), and number of constitutive elements (N). The entire cytoskeleton would then behave as a synergetic system of

spatially distributed polymeric elements working at different characteristic lengths and time scales.

ACKNOWLEDGEMENTS

This study was supported by the Institut National de la Santé et de la Recherche Médicale (Inserm) (Contract No. 4M106C, 1997-2000), the Centre National de la Recherche Scientifique (CNRS), Programme Physique et Chimie du Vivant (PCV98-097), and the Université Paris XII-Val de Marne (UPVM-Programme Pluri-formations 2000-2001).

APPENDIX

The various constitutive elements of the structure (referred to by the subscript "*p*" below) are defined by their geometrical dimensions (length L_p, radius r_p, cross-sectional area $S_p(=\pi r_p^2)$), and by their specific elastic properties, i.e., the Young modulus E_b constant for all bars, and E_c constant for all cables which are such that E_b is at least two orders of magnitude greater than E_c (subscript "*b*" will be used for bars and "*c*" for cables). T_b is the compressing force applied to rigid bars and T_c is the stretching force applied to cables. The stability of the tensegrity structure shape at reference state (i.e., in absence of external forces) results from the equilibrium between compressive and stretching internal forces. This leads to geometrical symmetries in tensegrity models at reference state (which however depend on both number of elements, attachment conditions and uniformity of initial tension in all cables), as previously demonstrated by Motro *et al.* (1990). Thus, at reference state, bar length, L_b, and cable length, L_c, are proportional whereas cables are equally pre-stretched and bars are equally pre-compressed, e.g., for the 30-element model at reference state, the bars are aligned in pairs in three perpendicular spatial planes, whereas $\frac{L_c^r}{L_b^r}=\frac{\sqrt{6}}{4}$. At the reference state, the tension (resp. the resulting compression), T_c (*resp*. T_b), is similar in every cable (*resp*. bar) in the structure and $\frac{T_c^r}{T_b^r}=\frac{\sqrt{6}}{6}$ (exponent "*r*" refers to reference state).

The internal tension of each structure (prestress) is characterised by a tension in each elastic cable which is assumed to be linearly related to initial strain (ε_c) (constant Young modulus in cables), i.e., $T_c = E_c S_c \varepsilon_c$. At reference state, this expression becomes $T_c^r = E_c S_c \varepsilon_c^r$, where ε_c^r is the initial extension in the cables.

When tensegrity models are submitted to different types of loading (traction, compression, shear), the resulting overall displacement may be calculated at small deformations (Wendling *et al*., 2000b) and large deformations (Wendling *et al*., 1999). Choosing for referential system the rectangular base $\{\vec{X},\vec{Y},\vec{Z}\}$, the *Z*-axis is the direction used to apply traction and compression forces, while the shear force was applied in the *Y*-axis direction. For instance, in the 30-element model, first order displacement of the upper bar through nodes {#6, #11} was calculated along the *Z*-axis, as a result of traction axial forces applied to nodes #6 and #11 in the *Z*-axis

direction. The global strain of the overall structure: $\varepsilon = \frac{\Delta u}{L_b^{(r)}}$ (Δu: relative nodal displacement), was deduced from the resolution of the following equation system:

$$\{F\} = [K]\{u\} \tag{A1}$$

which describes the equilibrium between the internal and external forces applied at each node.

For the 30-element model, the components of the column vector {F}, whose dimension is {1×36}, are the external forces applied at the 12 nodes of the structure in the three spatial directions. The components of the column vector {u} represent the resulting small nodal displacements in the three spatial directions. The overall rigidity matrix $[K]$ of the 30-element tensegrity structure (dimension {36×36}) is assembled from the rigidity matrices $[K]_p$ of the $p = 30$ individual elements (six rigid bars and 24 extensible cables). Each rigidity matrix $[K]_p$ may be written as the sum of (i) an elastic rigidity matrix $[K_E]_p$ function of physical characteristics of the element and the coordinates of the nodes, and (ii) a geometric rigidity matrix $[K_G]_p$, function of the actual stretching forces of the element and the nodal coordinates (Argyris and Scharpf, 1972). Thus, the matrix $[K]$ depends exclusively on the geometrical and mechanical properties of bars and cables.

For the 16-elements tensegrity model, it has been previously shown that the overall deformation is affine to a part of the structure reduced to a unique half long bar which is able to rotate while the other end is attached to three half long cables (Wendling *et al*., 2000a). In this particular case, an analytical solution can be used because the force F applied to the junction between the halved bar and the three halved cables reduces to a linear function of the angular bar position θ relative to the referential horizontal axis, i.e.,

$$F = E_c\, S_c\left(\sqrt{2}\tan\theta - 1\right). \tag{A2}$$

The applied force F appears independent of the initial extension of the cables ε_c, as far as stress-strain relationship characterizing cables remains linear (Wendling *et al*., 2000a).

For the two structures, the stress (traction, compression, shear) was obtained from the ratio of applied force to the mean cross-sectional area S_0 of the overall structure at reference state defined by: (i) $S_0 = \pi\left(L_0/2\right)^2$ corresponding to the cross-section area of a cylinder (diameter = height = $L_0 = L_b$) embedding the whole 30-element model, and (ii) $S_0 = \left(L_c^r\right)^2$ corresponding to the cross-sectional area of the cube (side length = $L_0 = L_c^r$) embedding the 16-element model. The apparent elasticity modulus (or structural stiffness) was defined by the stress/strain ratio at small deformation, i.e., $E = \sigma/\varepsilon$ with $\varepsilon = \Delta L_z/L_0$ and $\sigma = F/S_0$ in traction/compression and $E = \sigma/\gamma$ with

$\gamma = \Delta L_y / L_0$ in shear. The stress-strain relationship corresponding to Equation A2 may be written as follows:

$$\sigma = \frac{E_c S_c}{L_c^2 \cos\theta} \varepsilon + \frac{E_c S_c}{L_c^2 \cos\theta} \left(1 - \cos\theta\right) \tag{A3}$$

which is typically non-linear due to the θ-dependency of ε, and also inversely related to L^2.

REFERENCES

Albrecht Buehler, G. (1987). Role of cortical tension in fibroblast shape and movement. Cell Motility and the Cytoskeleton 7: 54 67.

Argyris, J.H., and D.W. Scharpf (1972). Large Deflection Analysis of Prestressed Networks. Journal of the Structural Division 106: 633 654.

Bausch, A.R., U. Hellerer, M. Essler, M. Aepfelbacher and E. Sackmann (2001). Rapid stiffening of integrin receptor actin linkages in endothelial cells stimulated with thrombin: a magnetic bead microrheology study. Biophysical Journal 80: 2649 2657.

Bausch, A.R., F. Ziemann, A.A. Boulbitch, K. Jacobson and E. Sackmann (1998). Local measurements of viscoelastic parameters of adherent cell surfaces by magnetic bead microrheometry. Biophysical Journal 75: 2038 2049.

Bretscher, A. (1991). Microfilament structure and function in the cortical cytoskeleton. Annual Reviews Cell & Developmental Biology 7: 337 374.

Caille, N., O. Thoumine, Y. Tardy and J.J. Meister (2002). Contribution of the nucleus to the mechanical properties of endothelial cells. Journal of Biomechanics 35: 177 187.

Cañadas, P., V.M. Laurent, C. Oddou, D. Isabey and S. Wendling (2002). A cellular tensegrity model to analyze the structural viscoelasticity of the cytoskeleton. Journal of Theoretical Biology 218: 155 173.

Chen, C.S., and D.E. Ingber (1999). Tensegrity and mechanoregulation: from skeleton to cytoskeleton. Osteoarthritis Cartilage 7: 81 94.

Cheng, Y., C.A. Hartemink, J.H. Hartwig and C.F. Dewey, Jr. (2000). Three dimensional reconstruction of the actin cytoskeleton from stereo images. Journal of Biomechanics 33: 105 113.

Chicurel, M.E., C.S. Chen and D.E. Ingber (1998). Cellular control lies in the balance of forces. Current Opinion in Cell Biology 10: 232 239.

Choquet, D., D.P. Felsenfeld and M.P. Sheetz (1997). Extracellular matrix rigidity causes strengthening of integrin cytoskeleton linkages. Cell 88: 39 48.

Coughlin, M.F., and D. Stamenovic (1997). A Tensegrity Structure with Buckling Compression Elements: Application to Cell Mechanics. Journal of Applied Mechanics 64: 480 486.

Discher, D.E., and N. Mohandas (1996). Kinematics of red cell aspiration by fluorescence imaged microdeformation. Biophysical Journal 71: 1680 1694.

Discher, D.E., N. Mohandas and E.A. Evans (1994). Molecular maps of red cell deformation: hidden elasticity and in situ connectivity. Science 266: 1032 1035.

Dong, C., R. Skalak and K.L. Sung (1991). Cytoplasmic rheology of passive neutrophils. Biorheology 28: 557 567.

Evans, E., and A. Yeung (1989). Apparent viscosity and cortical tension of blood granulocytes determined by micropipet aspiration. Biophysical Journal 56: 151 160.

Fabry, B., G. Maksym, R. Hubmayr, J. Butler and J. Fredberg (1999). Implications of heterogeneous bead behavior on cell mechanical properties measured with magnetic twisting cytometry. Journal of Magnetism and Magnetic Materials 194: 120 125.

Fox, J.E., and J.K. Boyles (1988). The membrane skeleton a distinct structure that regulates the function of cells. Bioessays 8: 14 18.

Fuller, R.B. (Ed.) (1975). Synergetics; Explorations of the geometry of thinking, Vol. 1. Macmillan Publishing Co, New York.
Fuller, R.B., and R. Marks (Eds) (1973). The Dymaxion World of Buckminster Fuller. Doubleday & Co., New York.
Fung, Y.C. (Ed.) (1981). Biomechanics; Mechanical properties of living tissues, Vol. 1. Springer Verlag, New York.
Gittes, F., B. Mickey, J. Nettleton and J. Howard (1993). Flexural Rigidity of Microtubules and Actin Filaments Measured from Thermal Fluctuations in Shape. The Journal of Cell Biology 120: 923 934.
Hamill, O.P., and B. Martinac (2001). Molecular basis of mechanotransduction in living cells. Physiological Reviews 81: 685 740.
Hartwig, J.H., and P. Shevlin (1986). The architecture of actin filaments and the ultrastructural location of actin binding protein in the periphery of lung macrophages. Journal of Cell Biology 103: 1007 1020.
Heidemann, S.R., S. Kaech, R.E. Buxbaum and A. Matus (1999). Direct observations of the mechanical behaviors of the cytoskeleton in living fibroblasts. Journal of Cell Biology 145: 109 122.
Hochmuth, R.M. (2000). Micropipette aspiration of living cells. Journal of Biomechanics 33: 15 22.
Hochmuth, R.M., and R.E. Waugh (1987). Erythrocyte membrane elasticity and viscosity. Annual Review of Physiology 49: 209 219.
Huang, S., and D.E. Ingber (2002). A discrete cell cycle checkpoint in late G(1) that is cytoskeleton dependent and MAP kinase (Erk) independent. Experimental Cell Research 275: 255 264.
Ingber, D.E. (1993). Cellular tensegrity: defining new rules of biological design that govern the cytoskeleton. Journal of Cell Science 104: 613 627.
Ingber, D.E. (1997). Tensegrity: the architectural basis of cellular mechanotransduction. Annual Review Of Physiology 59: 575 599.
Ingber, D.E. (2000). Opposing views on tensegrity as a structural framework for understanding cell mechanics. Journal of Applied Physiology 89: 1663 1670.
Ingber, D.E., and J.D. Jamieson (1985). Cells as tensegrity structures: architectural regulation of histodifferentiation by physical forces transduced over basement membrane. In: Andersson, L., C. Gahmberg and P. Ekblom (Eds). Gene expression during normal and malignant differentiation. Academic Press, Orlando: 13 32.
Ingber, D.E., L. Dike, L. Hansen, S. Karp, H. Liley, A. Maniotis, H. McNamee, D. Mooney, G. Plopper and J. Sims (1994). Cellular tensegrity: exploring how mechanical changes in the cytoskeleton regulate cell growth, migration, and tissue pattern during morphogenesis. International Review of Cytology 150: 173 224.
Ingber, D.E., J.A. Madri and J.D. Jamieson (1981). Role of basal lamina in the neoplastic disorganization of tissue architecture. Proceedings of the National Academy of Sciences of the United States of America: 3901 3905.
Janmey, P.A. (1998). The cytoskeleton and cell signaling: component localization and mechanical coupling. Physiological Reviews 78: 763 781.
Katoh, K., Y. Kano, M. Masuda, H. Onishi and K. Fujiwara (1998). Isolation and contraction of the stress fiber. Molecular Biology of the Cell 9: 1919 1938.
Katoh, K., M. Masuda, Y. Kano, Y. Jinguji and K. Fujiwara (1995). Focal adhesion proteins associated with apical stress fibers of human fibroblasts. Cell Motility and the Cytoskeleton 31: 177 195.
Laurent, V.M., S. Hénon, E. Planus, R. Fodil, M. Balland, D. Isabey and F. Gallet (2002). Assessment of mechanical properties of adherent living cells by bead micromanipulation: comparison of magnetic twisting cytometry *vs* optical tweezers. Journal of Biomechanical Engineering 124: 408 421.

Lodish, H., A. Berk, S.L. Zipursky, P. Matsudaira, D. Baltimore and J.E. Darnell (1999). Cell Motility and Shape. Molecular Cell Biology. 4th ed., W. H. Freeman and Company, New York.

Maniotis, A.J., C.S. Chen and D.E. Ingber (1997). Demonstration of mechanical connections between integrins, cytoskeletal filaments, and nucleoplasm that stabilize nuclear structure. Proceedings of the National Academy of Sciences of the United States of America 94: 849 854.

Mathur, A.B., G.A. Truskey and W.M. Reichert (2000). Atomic force and total internal reflection fluorescence microscopy for the study of force transmission in endothelial cells. Biophysical Journal 78: 1725 1735.

Motro, R. (1990). Tensegrity Systems and Geodesic Domes. International Journal of Space Structures 5: 341 351.

Needham, D., and R.M. Hochmuth (1992). A sensitive measure of surface stress in the resting neutrophil. Biophysical Journal 61: 1664 1670.

Planus, E., S. Galiacy, M. Matthay, V. Laurent, J. Gavrilovic, G. Murphy, C. Clérici, D. Isabey, C. Lafuma and M.P. d'Ortho (1999). Role of collagenase in mediating in vitro alveolar epithelial wound repair. Journal of Cell Science 112: 243 252.

Pourati, J., A. Maniotis, D. Spiegel, J.L. Schaffer, J.P. Butler, J.J. Fredberg, D.E. Ingber, D. Stamenovic and N. Wang (1998). Is cytoskeletal tension a major determinant of cell deformability in adherent endothelial cells? American Journal of Physiology 274: C1283 1289.

Pugh, A. (Ed.) (1976). Introduction to tensegrity. University of California Press, Berkeley.

Sato, M., M.J. Levesque and R.M. Nerem (1987). An application of the micropipette technique to the measurement of the mechanical properties of cultured bovine aortic endothelial cells. Journal of Biomechanical Engineering 109: 27 34.

Schmid Schonbein, G.W., T. Kosawada, R. Skalak and S. Chien (1995). Membrane model of endothelial cells and leukocytes. A proposal for the origin of a cortical stress. Journal of Biomechanical Engineering 117: 171 178.

Shafrir, Y., and G. Forgacs (2002). Mechanotransduction through the cytoskeleton. American Journal of Physiology Cell Physiology 282: C479 486.

Stamenovic, D., and M.F. Coughlin (1999). The Role of Prestress and Architecture of the Cytoskeleton and Deformability of Cytoskeletal in Mechanics of Adherent Cells: a Quantitative Analysis. Journal of Theoretical Biology 201: 63 74.

Stamenovic, D., and M.F. Coughlin (2000). A quantitative model of cellular elasticity based on tensegrity. Journal of Biomechanical Engineering 122: 39 43.

Stamenovic, D., D.E. Ingber, N. Wang and J.J. Fredberg (1996). A Microstructural Approach to Cytoskeletal Mechanics based on Tensegrity. Journal of Theoretical Biology 181: 125 136.

Thoumine, O. (1996). Control of Cellular Morphology by Mechanical Factors. Journal of Physics III 6: 1555 1566.

Wachsstock, D.H., W.H. Schwarz and T.D. Pollard (1994). Cross linker dynamics determine the mechanical properties of actin gels. Biophysical Journal 66: 801 809.

Wang, N. (1998). Mechanical interactions among cytoskeletal filaments. Hypertension 32: 162 165.

Wang, N., J.P. Butler and D.E. Ingber (1993). Mechanotransduction across the cell surface and through the cytoskeleton. Science 260: 1124 1127.

Wang, N., and D.E. Ingber (1994). Control of cytoskeletal mechanics by extracellular matrix, cell shape, and mechanical tension. Biophysical Journal 66: 2181 2189.

Wang, N., K. Naruse, D. Stamenovic, J.J. Fredberg, S.M. Mijailovich, I.M. Tolic Norrelykke, T. Polte, R. Mannix and D.E. Ingber (2001). Mechanical behavior in living cells consistent with the tensegrity model. Proceedings of the National Academy of Sciences of the United States of America 98: 7765 7770.

Wendling, S., C. Oddou and D. Isabey (1999). Stiffening response of a cellular tensegrity model. Journal of Theoretical Biology 196: 309 325.

Wendling, S., C. Oddou and D. Isabey (2000a). Approche Structurale de la mécanique du cytosquelette: solide alvéolaire vs modèle de tenségrité. Comptes Rendus de l'Académie des Sciences, Paris, 328 (Série IIb): 97 104.

Wendling, S., E. Planus, V.M. Laurent, L. Barbe, A. Mary, C. Oddou and D. Isabey (2000b). Role of cellular tone and microenvironmental conditions on cytoskeleton stiffness assessed by tensegrity model. The European Physical Journal Applied Physics 9: 51 62.

Yamada, S., D. Wirtz and S.C. Kuo (2000). Mechanics of living cells measured by laser tracking microrheology. Biophysical Journal l: 1736 1747.